Same macroscopic fields, different local mechanical loads: An electromechanical closure diagnostic

Bela Schulte Westhoff*

Technische Universität Berlin, 10587, Berlin, Germany

(Received 19 May 2026; revised 22 September 2026; accepted 8 October 2026; published 4 November 2026)

Continuum electromechanical models require bulk forces and surface tractions at the resolution of the target mechanical prediction. Agreement in macroscopic-electromagnetic fields, or even in total force, does not by itself establish that these local loads are determined. Starting from microscopic carrier balances, we formulate an output-first minimum-closure diagnostic that separates two ordered questions: transmission closure $\mathcal{C}_T$ specifies how Lorentz forces on carriers reach the selected mechanical host, whereas projection closure $\mathcal{C}_P$ asks whether the retained electromagnetic state determines the required load once transmission is fixed. Two controlled equal-state comparisons isolate these noninterchangeable failure modes. In a uniform prescribed external field, bound dipoles and individually anchored charges have the same retained electromagnetic state and retained projection of the applied-field carrier loading, yet produce different host loads because their support topologies transmit end point forces differently. With transmission fixed, aligned and staggered line-dipole arrangements have the same retained polarization and continuum field, yet produce different boundary tractions because registry-dependent near-field correlations omitted by retention survive as an interfacial load. These witnesses establish structural nonuniqueness within the declared model classes, rather than universal material magnitudes. The diagnostic stops when global balance fixes the requested total force or torque on the receiving system; otherwise, it establishes transmission before testing whether a projection residual affects the selected output above tolerance. Missing closure may be supplied by a support or carrier-kinetic model, targeted reconstruction, or an equivalent validated reduced law. A macroscopic load law is therefore sufficient whenever transmission is fixed or irrelevant, and all output-relevant residuals are negligible or represented.

DOI: 10.1103/8s4n-1fvh

I. INTRODUCTION AND SCOPE

To predict motion or deformation, a continuum-mechanical model requires the force supplied by the electromagnetic subsystem. Its local momentum balance may be written schematically as:

$$\rho\mathbf{a} = \nabla\cdot\boldsymbol{\sigma}_{\mathrm{mech}} + \mathbf{f}_{\mathrm{other}} + \mathbf{f}_{\mathrm{em}}. \tag{1}$$

Here ρ is the continuum mass density, $\mathbf{a}$ is the material acceleration of the continuum velocity $\mathbf{v}$, and $\mathbf{f}_{\mathrm{other}}$ is the force density assigned to other loading channels in the selected balance. The tensor $\boldsymbol{\sigma}_{\mathrm{mech}}$ denotes the constitutive stress assigned to the selected mechanical model, whereas $\mathbf{f}_{\mathrm{em}}$ denotes the load transferred from the selected electromagnetic ledger. This partition concerns their roles in the continuum model, not the microscopic origin of the interactions. Depending on the formulation, this load may enter as bulk force densities and boundary tractions or through an electromagnetic stress. The required resolution of $\mathbf{f}_{\mathrm{em}}$ is set by the selected output and target accuracy, not necessarily by the electromagnetic field resolution. Equation (1) is therefore understood in the weak or distributional sense.

The spatial distribution of this load matters whenever the requested output depends on deformation rather than only on a total resultant. Two modeling workflows that predict the same total force but different spatial distributions of bulk force and surface traction can yield different stress, strain, interface shape, modal amplitude, or fracture response. Experiments and established interface models demonstrate the output relevance of local loading in optical modal response and measured deformation [1,2], transiently separated bulk and surface forces [3], drop-interface shape [4], crack-face traction [5], and piezoelectret response [6]. Coupled electromagnetic-deformation models in biological cells provide a broader continuum setting [7]. Electroelastic, ferroelectric, and magnetoelastic models encode the same handoff

*Contact author: schultewesthoff@tu-berlin.de

Published by the American Physical Society under the terms of the Creative Commons Attribution 4.0 International license. Further distribution of this work must maintain attribution to the author(s) and the published article's title, journal citation, and DOI.

through deformation-dependent energies, eigenstrains, domain variables, or multiscale laws [8–13].

For local mechanical loading, macroscopic-electromagnetic fields may be insufficient on their own. We call the additional material, constitutive, boundary, or microstructural information needed to determine $\mathbf{f}_{\mathrm{em}}$ for a specified material class and output *closure*. Equation (1) locates the electromagnetic load in the mechanical balance but does not, by itself, specify the material-specific map from the retained electromagnetic state to that load. Established models provide such closure through three main routes: a deformation-dependent energy or electromechanical constitutive law; direct microscopic or multiscale reconstruction of the relevant carriers, supports, and interfaces; or experimental model validation or inverse calibration for a stated material, geometry, loading range, and output [3,8,14–27].

Prior work provides separate foundations for the present analysis: species-resolved balances and common-relative kinematics; recipient- and scale-dependent representations of mechanical force; and micro-to-continuum treatments that reveal unresolved correlation, lattice, and termination effects [16,17,23,24,28–35]. These strands show that successful field propagation, momentum accounting, or total-force prediction need not determine the local deformation load [16,25,30,32,36–38], whose mechanical consequences are documented in interfacial and modal settings [1,4,39,40]. What is missing is a single output-conditioned factorization of the carrier-to-continuum load handoff that distinguishes missing carrier-to-host transmission closure from insufficient spatial information in the retained electromagnetic state. We make this distinction explicit through the four-stage construction below, from a poststability ion-electron reference model to the continuum load $\mathbf{f}_{\mathrm{em}}$ in Eq. (1). To diagnose retained-state sufficiency separately, transmission must first be fixed or rendered irrelevant; an initial model may require both closures, while either issue requires additional closure only if it affects the declared output above tolerance:

$$\begin{aligned}
&(1)\ \text{Full microscopic carrier balances}\\
&\qquad\xrightarrow{\text{kinematic organization}}\\
&(2)\ \text{Selected carrier ledger and host } H(\mathbf{v})\\
&\qquad\xrightarrow{\text{transmission } \mathcal{C}_T}\\
&(3)\ \text{Microscopic host load } \mathbf{f}_H^{\mathrm{mic}}\\
&\qquad\xrightarrow{\text{continuum retention}}\\
&(4)\ \text{Retained continuum load } \mathbf{f}_{\mathrm{em}}.
\end{aligned} \tag{2}$$

Stage (1) is the full microscopic carrier reference model. The first transition introduces a chosen, lossless organization of the same carrier motion into fluctuation, common-motion, and charge-relative roles. Stage (2) thereby identifies the continuum host $H(\mathbf{v})$ as the mechanical recipient and the relevant carrier Lorentz-force ledger as the electromagnetic load source; how that load is transmitted to the host remains to be specified.

Stage (2) to stage (3) is the transmission step. The relation $\mathcal{C}_T$ specifies how the selected carrier load is delivered through binding, anchoring, or other supports to the continuum host $H(\mathbf{v})$, producing the microscopic host load $\mathbf{f}_H^{\mathrm{mic}}$. We isolate this closure with a transmission witness: an equal-retained-projection pair with different admissible support relations produces different host loads.

Stage (3) to stage (4) is the continuum-retention step, which represents $\mathbf{f}_H^{\mathrm{mic}}$ at the resolution of the mechanical model as $\mathbf{f}_{\mathrm{em}}$. Projection closure $\mathcal{C}_P$ denotes the additional relation or information, if any, required to infer that retained load from the retained electromagnetic state once transmission, the microscopic host-load law, and mechanical retention are fixed. We isolate this closure with a projection witness: after fixing transmission, two admissible microscopic realizations share the retained electromagnetic state but produce different local mechanical loads. Together, the four-stage factorization is conditionally exhaustive for missing closure in this declared load handoff: once the reference model, selected carrier ledger, receiving host, declared output, and continuum-retention convention are fixed, any remaining closure need enters either the stage (2)-to-stage (3) transmission map $\mathcal{C}_T$ or, after transmission and the microscopic host-load law are fixed, the retained-state inference $\mathcal{C}_P$. The two closures are noninterchangeable but not mutually exclusive: an initial model may require both, and $\mathcal{C}_P$ can be tested separately only after $\mathcal{C}_T$ is fixed or irrelevant. This exhaustiveness is conditional on the declared material class, mechanical output, resolution, and target accuracy; deficiencies of the reference model, constitutive mechanics, or numerical approximation lie outside the closure classification.

Accordingly, the contribution is the linked, ordered, output-conditioned factorization and operationalization of these ingredients; novelty is not claimed for any individual carrier balance, kinematic split, dipole identity, microstructure-sensitive force effect, or multiscale method. The diagnostic has four linked elements: a lossless kinematic organization that identifies the selected carrier ledger and mechanical recipient before closure; the ordered factorization into $\mathcal{C}_T$ and $\mathcal{C}_P$, isolated by equal-retained-state witnesses; localization of the bulk and interfacial projection residual, with a matched actual-minus-smooth reconstruction in the line-dipole benchmark; and an output- and tolerance-dependent audit that states when further closure is unnecessary and what kind of information is required when it is not. Together, these elements make a failed state-to-load inference localizable and identify the type of additional closure information required for the selected task.

Our diagnostic does not rank or replace established electromagnetic force and stress expressions, which may be appropriate for their intended balance-law, momentum-bookkeeping, total-force, or constitutive purposes [16,17,29,41–43]. It asks the narrower question of whether a chosen expression determines the local mechanical load for the declared receiving system, material class, output, resolution, and tolerance. If so, no further closure is required for that task; if not, the framework locates the missing information in $\mathcal{C}_T$, $\mathcal{C}_P$, or both.

Section II develops the reference model and identifies the microscopic load source and continuum-mechanical recipient; Sec. III defines the retained electromagnetic state and continuum load and poses the remaining closure question. Sections IV and V test $\mathcal{C}_T$ and $\mathcal{C}_P$, respectively, and Sec. VI formulates the minimum-closure audit and the corresponding routes to closure.

II. BASE-RESOLUTION MODEL AND ELECTROMECHANICAL HANDOFF

Equation (1) requires an electromagnetic load on the continuum motion $\mathbf{v}$, whereas microscopic electrodynamics supplies Lorentz forces on ions and electrons. This section fixes the microscopic carrier reference model and then adopts a lossless kinematic organization to distinguish the roles used in the thermodynamic, continuum-mechanical, and macroscopic-electromagnetic descriptions. The resulting stage (2) identifies the selected carrier Lorentz-force ledger as the load source and $H(\mathbf{v})$ as the mechanical recipient; no continuum retention or load transmission occurs here.

A. Base-resolution carrier model

To define the microscopic source of the handoff, we represent matter at stage (1) by two massive charged carrier species,

$$a \in \{i, e\}, \qquad q_i > 0, \qquad q_e < 0, \tag{3}$$

where a is a species index and i and e denote ions and electrons. Charge densities below carry a species or source label and are distinct from the mass density ρ in Eq. (1). Species a has number density n_a^{mic}, mass m_a, charge q_a, and velocity $\mathbf{u}_a^{\mathrm{mic}}$. Its charge, current, and mechanical-momentum densities are

$$\begin{aligned} \rho_a^{\mathrm{mic}} &= q_a n_a^{\mathrm{mic}}, \\ \mathbf{j}_a^{\mathrm{mic}} &= \rho_a^{\mathrm{mic}} \mathbf{u}_a^{\mathrm{mic}}, \\ \mathbf{g}_a^{\mathrm{mic}} &= m_a n_a^{\mathrm{mic}} \mathbf{u}_a^{\mathrm{mic}}. \end{aligned} \tag{4}$$

Charge and mass therefore weight the same carrier motion differently: charge weights the electromagnetic source terms, whereas mass weights the mechanical momentum.

The carriers interact with the microscopic electric field $\mathbf{e}_{\mathrm{mic}}$ and magnetic induction $\mathbf{b}_{\mathrm{mic}}$. The Lorentz-force density on each species is

$$\begin{aligned} \mathbf{f}_{\mathrm{L},a}^{\mathrm{mic}} &= \rho_a^{\mathrm{mic}} \mathbf{e}_{\mathrm{mic}} + \mathbf{j}_a^{\mathrm{mic}} \times \mathbf{b}_{\mathrm{mic}} \\ &= q_a n_a^{\mathrm{mic}} (\mathbf{e}_{\mathrm{mic}} + \mathbf{u}_a^{\mathrm{mic}} \times \mathbf{b}_{\mathrm{mic}}). \end{aligned} \tag{5}$$

Summing over the two carrier species gives the total microscopic electromagnetic loading,

$$\mathbf{f}_{\mathrm{L}}^{\mathrm{mic}} = \sum_{a=i,e} \mathbf{f}_{\mathrm{L},a}^{\mathrm{mic}} = \rho_{\mathrm{mic}} \mathbf{e}_{\mathrm{mic}} + \mathbf{j}_{\mathrm{mic}} \times \mathbf{b}_{\mathrm{mic}}, \tag{6}$$

where $\rho_{\mathrm{mic}} = \sum_a \rho_a^{\mathrm{mic}}$ and $\mathbf{j}_{\mathrm{mic}} = \sum_a \mathbf{j}_a^{\mathrm{mic}}$.

We use an effective poststability reference in which stable ionic and electronic configurations are taken as given. Quantum-scale stabilization is not modeled explicitly; its effects are absorbed into the admissible configurations and the effective non-Lorentz constraint-support reaction $\mathbf{f}_{\mathrm{con},a}^{\mathrm{mic}}$, which also includes imposed binding or anchoring reactions [28,29]. The explicit dynamics are then massive-carrier mechanics coupled to microscopic Maxwell–Lorentz electrodynamics [42,44], with species momentum balances:

$$\frac{\partial \mathbf{g}_a^{\mathrm{mic}}}{\partial t} + \nabla \cdot \mathbf{t}_{\mathrm{kin},a}^{\mathrm{mic}} = \mathbf{f}_{\mathrm{L},a}^{\mathrm{mic}} + \mathbf{f}_{\mathrm{con},a}^{\mathrm{mic}}, \qquad a \in \{i, e\}. \tag{7}$$

Here t is time and $\mathbf{t}_{\mathrm{kin},a}^{\mathrm{mic}}$ is the kinetic momentum-flux tensor of species a, whose divergence accounts for transport of that species momentum. Their sum gives the base-resolution matter ledger:

$$\frac{\partial \mathbf{g}_{\mathrm{mech}}^{\mathrm{mic}}}{\partial t} + \nabla \cdot \mathbf{t}_{\mathrm{kin}}^{\mathrm{mic}} = \mathbf{f}_{\mathrm{L}}^{\mathrm{mic}} + \mathbf{f}_{\mathrm{con}}^{\mathrm{mic}}, \tag{8}$$

with $\mathbf{g}_{\mathrm{mech}}^{\mathrm{mic}} = \sum_a \mathbf{g}_a^{\mathrm{mic}}$, $\mathbf{t}_{\mathrm{kin}}^{\mathrm{mic}} = \sum_a \mathbf{t}_{\mathrm{kin},a}^{\mathrm{mic}}$, and $\mathbf{f}_{\mathrm{con}}^{\mathrm{mic}} = \sum_a \mathbf{f}_{\mathrm{con},a}^{\mathrm{mic}}$. Equations (3)–(8) therefore specify the complete microscopic carrier ledger, the common carrier-side basis of the three multiphysics roles organized below. Connecting this ledger to Eq. (1) requires identifying both the continuum coordinate that receives the load and the selected Lorentz-force contribution that supplies the microscopic source of $\mathbf{f}_{\mathrm{em}}$; neither identification follows from the ledger alone. Assuming this effective classical reference is adequate for the selected output and accuracy, we now introduce this chosen kinematic organization.

B. Kinematic organization of carrier motion

The base-resolution carrier ledger contains the carrier motion to be organized, but the species velocities $\mathbf{u}_a^{\mathrm{mic}}$ do not uniquely prescribe that organization. We therefore adopt three roles: fluctuations enter thermodynamic moments and kinetic stress, common material motion

defines the selected continuum-mechanical coordinate, and ordered charge-relative motion contributes to macroscopic current and polarization. Once defined, the transformation is lossless; no continuum retention or load closure occurs. Write the microscopic velocity of each species as an ordered velocity $\mathbf{U}_a$ plus an unordered fluctuation $\mathbf{c}_a$,

$$\mathbf{u}_a^{\mathrm{mic}} = \mathbf{U}_a + \mathbf{c}_a, \qquad \langle n_a^{\mathrm{mic}} \mathbf{c}_a \rangle = \mathbf{0}. \tag{9}$$

Once $\mathbf{U}_a$ and $\mathbf{c}_a$ are defined, Eq. (9) is an identity; the unsubscripted bracket denotes the local carrier-moment average used in the split, distinct from the spatial-retention average $\langle\cdot\rangle_\ell$ introduced below. The fluctuations remain explicit and continue to enter thermodynamic variables and kinetic stresses, so no microscopic information has been removed. For the ordinary nonrelativistic solids and dielectrics considered here, we take the ionic ordered velocity as the common continuum velocity and resolve the electron motion relative to it:

$$\mathbf{U}_i = \mathbf{v}, \qquad \mathbf{U}_e = \mathbf{v} + \mathbf{w}, \qquad \mathbf{w} = \dot{\boldsymbol{\xi}}, \tag{10}$$

Here $\boldsymbol{\xi}$ is the ordered electron displacement relative to the ionic skeleton, $\mathbf{w}$ is its relative velocity, and the overdot denotes its time derivative following that skeleton.

Let ρ_i^{ord} and ρ_e^{ord} denote the ionic and electronic charge densities associated with the ordered sector. Its current is

$$\begin{aligned} \mathbf{J}_{\mathrm{ord}} &= \rho_i^{\mathrm{ord}} \mathbf{U}_i + \rho_e^{\mathrm{ord}} \mathbf{U}_e = \rho_{\mathrm{ord}} \mathbf{v} + \rho_e^{\mathrm{ord}} \mathbf{w}, \\ \rho_{\mathrm{ord}} &= \rho_i^{\mathrm{ord}} + \rho_e^{\mathrm{ord}}. \end{aligned} \tag{11}$$

Equation (11) makes the electrodynamic role of the decomposition explicit. For a locally neutral ordered sector, $\rho_{\mathrm{ord}} = 0$, so common ion-electron motion produces no net charge current. Ordered relative motion produces the current, while a persistent relative displacement $\boldsymbol{\xi} \neq \mathbf{0}$ produces charge separation and polarization even when $\mathbf{w} = \mathbf{0}$. If ordered net charge is present, the convection term $\rho_{\mathrm{ord}}\mathbf{v}$ remains explicitly. Unordered relative motion may still generate microscopic current and field fluctuations, but it does not enter $\mathbf{J}_{\mathrm{ord}}$ because its defining local first moment vanishes. These fluctuations remain in the microscopic state; no spatial retention has yet been applied.

The corresponding ordered mechanical-momentum density is

$$\mathbf{g}_{\mathrm{ord}} = \rho_{m,i}^{\mathrm{ord}} \mathbf{v} + \rho_{m,e}^{\mathrm{ord}} (\mathbf{v} + \mathbf{w}) = \rho_m^{\mathrm{ord}} \mathbf{v} + \rho_{m,e}^{\mathrm{ord}} \mathbf{w} \simeq \rho_m^{\mathrm{ord}} \mathbf{v}. \tag{12}$$

Here $\rho_{m,i}^{\mathrm{ord}}$ and $\rho_{m,e}^{\mathrm{ord}}$ are the ionic and electronic mass densities associated with the ordered sector, and $\rho_m^{\mathrm{ord}} = \rho_{m,i}^{\mathrm{ord}} + \rho_{m,e}^{\mathrm{ord}}$. The final approximation uses $\rho_{m,e}^{\mathrm{ord}} \ll \rho_{m,i}^{\mathrm{ord}}$. Equation (12) makes the mechanical role explicit: the common material momentum is dominated by the ionic skeleton, although the electron mass remains in the relative-motion momentum. The superscript ord labels a kinematic role, not a retained continuum field; the fluctuation sector remains part of the state, and no spatial information has yet been removed.

Together, Eqs. (9) and (10) organize the same microscopic carrier motion into the three roles used in the present construction,

$$\begin{aligned} \{\mathbf{u}_i^{\mathrm{mic}}, \mathbf{u}_e^{\mathrm{mic}}\} &\Longleftrightarrow \{\mathbf{c}_i, \mathbf{c}_e, \mathbf{v}, \mathbf{w}\}, \\ \{\mathbf{c}_i, \mathbf{c}_e\} &\rightarrow \text{fluctuation sector}, \\ \mathbf{v} &\rightarrow \text{common-motion sector}, \\ (\boldsymbol{\xi}, \mathbf{w}) &\rightarrow \text{charge-relative sector}. \end{aligned} \tag{13}$$

Equation (13) completes this chosen, lossless kinematic organization. The common-motion variable $\mathbf{v}$ identifies the material coordinate of the receiving host $H(\mathbf{v})$, whose continuum balance is Eq. (1). The ordered charge-relative variables identify the carrier charge and current associated with the selected microscopic Lorentz-force ledger $\mathbf{f}_{\mathrm{L,sel}}^{\mathrm{mic}}$. For each declared comparison, this symbol denotes the specified carrier and field contribution of the full stage (1) Lorentz ledger whose transfer is being audited; in Mechanism I, it is the prescribed external-field contribution. This ledger is the microscopic electromagnetic load source from which $\mathbf{f}_{\mathrm{em}}$ in Eq. (1) must ultimately be constructed.

Section II therefore completes the transition from stage (1) to stage (2): it identifies the receiving mechanical host and the microscopic electromagnetic load source. It has not yet specified how that source loading reaches the host or how the resulting load is represented at continuum resolution. Section III next defines the retained field state and mechanical load. With those definitions in place, Sec. IV examines the stage (2)-to-stage (3) transmission $\mathcal{C}_T$, and Sec. V examines the stage (3)-to-stage (4) inference $\mathcal{C}_P$.

III. CONTINUUM RETENTION OF FIELDS AND LOADS

Section II organized the microscopic carrier-field system without information loss. Continuum retention instead maps distinct microstates to the same macrostate, with each domain retaining different information and encoding the rest constitutively.

This section defines the needed projections. Section III A separates sources and fields into retained quantities and complements, establishing electromagnetic equivalence. Section III B takes $\mathbf{f}_H^{\mathrm{mic}}$ as given and defines the retained bulk force density and surface traction. These

form the state and load target for comparisons in Secs. IV and V.

A. Electromagnetic retention and retained field equations

Microscopic starting point. In the effective reference model of Sec. II, the microscopic sources and fields obey

$$\begin{aligned}\nabla\cdot\mathbf{e}_{\mathrm{mic}} &= \frac{\rho_{\mathrm{mic}}}{\epsilon_0},\\ \nabla\times\mathbf{e}_{\mathrm{mic}} &= -\partial_t\mathbf{b}_{\mathrm{mic}},\\ \nabla\cdot\mathbf{b}_{\mathrm{mic}} &= 0,\\ \nabla\times\mathbf{b}_{\mathrm{mic}} &= \mu_0\mathbf{j}_{\mathrm{mic}}+\mu_0\epsilon_0\partial_t\mathbf{e}_{\mathrm{mic}}.\end{aligned} \tag{14}$$

Here ϵ_0 and μ_0 are the vacuum permittivity and permeability. Equation (14) is the microscopic field description before continuum retention. Its solutions contain continuum-scale variation and microscopic carrier-scale structure, including localized near fields. The retained macroscopic state instead represents field content at the declared resolution and accuracy. We define retention below for smooth bulk and unresolved interfaces; whether omitted structure affects the retained mechanical load is a separate question.

Scale-separated retention in smooth bulk. Away from boundaries, the microscopic sources and fields contain rapidly varying components on an atomic or lattice scale d_{mic}, whereas the retained macroscopic fields vary over a much larger resolved scale L_{EM}. In the macroscopic systems considered here, these scales are typically separated by many orders of magnitude. Writing k for spatial wave number, the corresponding characteristic wave numbers satisfy $k_{\mathrm{EM}}\sim L_{\mathrm{EM}}^{-1}\ll k_{\mathrm{mic}}\sim d_{\mathrm{mic}}^{-1}$, leaving a wide intermediate range. Macroscopic retention can consequently be defined using any mesoscopic averaging length ℓ, or equivalently cutoff $k_c\sim\ell^{-1}$, within this range:

$$d_{\mathrm{mic}}\ll\ell\ll L_{\mathrm{EM}}\Longleftrightarrow k_{\mathrm{EM}}\ll k_c\ll k_{\mathrm{mic}}. \tag{15}$$

Every such averaging scale spans many microscopic cells while remaining too small to blur the resolved field. Accordingly, varying ℓ, the cutoff position, or the precise shape of a reasonable averaging kernel changes the retained fields only below the target accuracy. This broad range of equivalent coarse-grainings is the *bulk averaging plateau*; no unique averaging length or cutoff is required.

On this plateau, a normalized mesoscopic kernel K_ℓ defines retention of a generic microscopic quantity a_{mic} and its residual δa. With observation position $\mathbf{x}$ and integration position $\mathbf{r}$,

$$a_{\mathrm{ret}}(\mathbf{x},t)\equiv\langle a_{\mathrm{mic}}\rangle_\ell=\int K_\ell(\mathbf{x}-\mathbf{r})a_{\mathrm{mic}}(\mathbf{r},t)d^3r, \tag{16}$$

$$a_{\mathrm{mic}}=a_{\mathrm{ret}}+\delta a,\qquad \langle\delta a\rangle_\ell\simeq 0. \tag{17}$$

The retained electric field $\mathbf{E}$, magnetic induction $\mathbf{B}$, charge density ρ_{macro}, and current density $\mathbf{J}_{\mathrm{macro}}$ are

$$\begin{aligned}\mathbf{E}&=\langle\mathbf{e}_{\mathrm{mic}}\rangle_\ell, & \mathbf{B}&=\langle\mathbf{b}_{\mathrm{mic}}\rangle_\ell,\\ \rho_{\mathrm{macro}}&=\langle\rho_{\mathrm{mic}}\rangle_\ell, & \mathbf{J}_{\mathrm{macro}}&=\langle\mathbf{j}_{\mathrm{mic}}\rangle_\ell.\end{aligned} \tag{18}$$

Mechanism II tests whether spatial structure omitted from the retained electromagnetic state can nevertheless contribute to the retained mechanical load.

Unresolved interfaces. Across a microscopic material interface, the sources and fields vary rapidly through the transition layer and contain a broad range of spatial wave numbers. There is therefore no unique local low-k and high-k separation and no position-insensitive averaging plateau. Consequently, an averaging window crossing the layer samples both phases, and the resulting continuum profile depends on the kernel, averaging length, window position, and microscopic termination. The convention adopted here replaces the microscopic transition layer with prescribed bulk profiles on either side, a sharp interface, and the associated surface sources and jump conditions. For example, a body with constant bulk polarization $\mathbf{P}_0$ and sharp polarization profile $\mathbf{P}(\mathbf{r})=\mathbf{P}_0\chi_\Omega(\mathbf{r})$ carries

$$-\nabla\cdot(\mathbf{P}_0\chi_\Omega)=(\hat{\mathbf{n}}\cdot\mathbf{P}_0)\delta_{\partial\Omega}, \tag{19}$$

where χ_Ω equals one inside the continuum body Ω and zero outside, $\hat{\mathbf{n}}$ is the outward unit normal, and $\delta_{\partial\Omega}$ is the surface delta distribution. Because the prescribed profile is discontinuous, it contains high-k content and is not a purely low-pass field. This content does not represent retained microscopic detail; it represents the sharp interface and its integrated polarization jump.

At an unresolved interface, a_{ret} is not the convolution in Eq. (16) but the prescribed sharp-interface representation, and $\delta a\equiv a_{\mathrm{mic}}-a_{\mathrm{ret}}$ is the omitted transition-layer correction. Because a_{ret} contains jump-induced high-k content, this is not a clean low-k and high-k split; $\langle\delta a\rangle_\ell\simeq 0$ is therefore not imposed across the layer. Under scale separation, the sharp model reproduces the resolved exterior fields and continuum jumps, but not the pointwise transition-layer field.

Maxwell form after retention. For a fixed translation-invariant, time-independent kernel and a generic field a,

$$\langle\nabla a\rangle_\ell=\nabla\langle a\rangle_\ell,\qquad \langle\partial_t a\rangle_\ell=\partial_t\langle a\rangle_\ell.$$

Averaging Eq. (14) therefore gives

$$\begin{aligned}\nabla\cdot\mathbf{E} &= \frac{\rho_{\mathrm{macro}}}{\epsilon_0},\\ \nabla\times\mathbf{E} &= -\partial_t\mathbf{B},\\ \nabla\cdot\mathbf{B} &= 0,\\ \nabla\times\mathbf{B} &= \mu_0\mathbf{J}_{\mathrm{macro}} + \mu_0\epsilon_0\partial_t\mathbf{E}.\end{aligned} \tag{20}$$

Linearity and derivative commutation preserve the Maxwell form in smooth bulk. This does not require a linear material closure; constitutive relations and boundary data are still needed to complete the retained problem.

To connect the retained sources with the conventional material fields used below, consider a selected neutral source subset whose microscopic charge separation and current circulation may be represented by:

$$\rho_{\mathrm{rep}} = -\nabla\cdot\mathbf{p}_{\mathrm{mic}}, \qquad \mathbf{j}_{\mathrm{rep}} = \partial_t\mathbf{p}_{\mathrm{mic}} + \nabla\times\mathbf{m}_{\mathrm{mic}}. \tag{21}$$

Here ρ_{rep} and $\mathbf{j}_{\mathrm{rep}}$ are the charge and current densities of the selected subset and $\mathbf{p}_{\mathrm{mic}}$ and $\mathbf{m}_{\mathrm{mic}}$ represent its microscopic polarization and magnetization. These are source-bookkeeping fields, not additional substances or a mechanical host. Their averages define the retained polarization $\mathbf{P} = \langle\mathbf{p}_{\mathrm{mic}}\rangle_\ell$ and magnetization $\mathbf{M} = \langle\mathbf{m}_{\mathrm{mic}}\rangle_\ell$. With electric displacement $\mathbf{D} = \epsilon_0\mathbf{E} + \mathbf{P}$ and magnetic field intensity $\mathbf{H} = \mathbf{B}/\mu_0 - \mathbf{M}$, and with the remaining sources classified separately, Eq. (20) can be written in the familiar macroscopic $\mathbf{D}, \mathbf{H}$ form.

For the equal-state comparisons below, we collect the retained electromagnetic variables of a microscopic realization x as:

$$\mathbf{S}_{\mathrm{EM}}(x) = (\mathbf{E}, \mathbf{P}, \mathbf{D}, \mathbf{B}, \mathbf{H}, \mathbf{M}). \tag{22}$$

This tuple is deliberately redundant: its entries need not be independent. In smooth bulk, two microscopic realizations are electromagnetically equivalent at the declared resolution when they have the same retained state. Their complements may still contain different microscopic charge geometry, registry, currents, and near fields. In particular, different microscopic complements $\delta\mathbf{p}^{(1)}$ and $\delta\mathbf{p}^{(2)}$, defined by $\delta\mathbf{p} = \mathbf{p}_{\mathrm{mic}} - \mathbf{P}$, can accompany the same $\mathbf{P}$ and hence the same retained source footprint $-\nabla\cdot\mathbf{P}$. At an unresolved interface, equality instead means that the realizations share the prescribed bulk profiles and Maxwell boundary problem, not the same microscopic transition layer.

The retained Maxwell problem thus describes slowly varying fields in smooth bulk and the resolved fields and jumps associated with prescribed sharp interfaces. It omits microscopic near fields and transition-layer structure that are unnecessary for the declared field accuracy. It therefore establishes electromagnetic equivalence, not mechanical-load equivalence: it does not determine carrier topology, binding, or anchoring or how microscopic loading reaches the continuum body. The next subsection defines the retained mechanical load and poses whether the electromagnetic state determines it.

B. Retained continuum load and closure question

To prepare the two later comparisons, we first define the continuum-retention step from stage (3) to stage (4). Let $\mathbf{f}_H^{\mathrm{mic}}$ denote the microscopic load delivered to the receiving host $H(\mathbf{v})$:

$$\mathbf{f}_H^{\mathrm{mic}} \xrightarrow{\text{continuum retention}} \mathbf{f}_{\mathrm{em}}. \tag{23}$$

Unlike electromagnetic field retention, mechanical retention is set by the selected mechanical output. In smooth bulk, $\mathbf{f}_H^{\mathrm{mic}}$ contains variations on the atomic or lattice scale d_{mic}, whereas the retained deformation varies over a much larger scale L_{mech}. Force structure outside the retained mechanical band may be filtered out when it does not change that output above the target accuracy. If $d_{\mathrm{mic}} \ll \ell_{\mathrm{mech}} \ll L_{\mathrm{mech}}$, averaging over many microscopic cells gives a stable bulk load. At a microscopic interface, the averaging window instead mixes both phases and the terminating force layer, so no unique local plateau needs to exist. We therefore retain

$$\begin{aligned}\mathbf{f}_{\mathrm{em}}^{\mathrm{bulk}} &\simeq \langle\mathbf{f}_H^{\mathrm{mic}}\rangle_{\ell_{\mathrm{mech}}} \text{ in smooth bulk,}\\ \mathbf{t}_{\mathrm{em}} &\simeq \int_{\text{unresolved layer}} \mathbf{f}_H^{\mathrm{mic}}\, d\,n \text{ at a sharp interface.}\end{aligned} \tag{24}$$

Here n is distance normal to the interface, $\mathbf{f}_{\mathrm{em}}^{\mathrm{bulk}}$ is force per unit volume, and $\mathbf{t}_{\mathrm{em}}$ is force per unit area. The first line removes fine bulk oscillations under this output criterion. At an interface, the detailed normal profile is convention-dependent, but its integral is retained as the surface traction representing the resolved action of the force layer. The continuum input is therefore the pair $(\mathbf{f}_{\mathrm{em}}^{\mathrm{bulk}}, \mathbf{t}_{\mathrm{em}})$.

Equation (24) defines the retained continuum load once $\mathbf{f}_H^{\mathrm{mic}}$ is known. Section IV first examines the preceding stage (2)-to-stage (3) transmission step. Section V then uses a controlled example to test whether the retained electromagnetic state determines the stage (3)-to-stage (4) load.

IV. MECHANISM I: CARRIER-TO-HOST TRANSMISSION

Section II identified the two microscopic participants in the electromechanical handoff: the selected ionic and electronic carriers on which the Lorentz forces act, and the mechanical host $H(\mathbf{v})$ that must receive their load. Section III then defined how the resulting host load is retained at continuum resolution. What remains

undetermined is the prior transmission from carriers to host. Does the microscopic carrier loading act directly on the selected host coordinate, or is it redistributed by binding, anchoring, or other supports before reaching that coordinate? This question arises before continuum retention. We therefore isolate the stage (2)-to-stage (3) transmission step for the incremental load produced by a prescribed external field:

$$\underbrace{\mathbf{f}^{\mathrm{mic}}_{\mathrm{L,sel}}}_{\substack{\text{stage (2):}\\ \text{carrier loading}}} \xrightarrow{\mathcal{C}_T} \underbrace{\mathbf{f}^{\mathrm{mic}}_{H}}_{\text{stage (3)}} \xrightarrow{\text{continuum retention}} \underbrace{\mathbf{f}_{\mathrm{em}}}_{\text{stage (4)}} . \tag{25}$$

In this section, $\mathbf{e}_{\mathrm{ext}}$ and $\mathbf{b}_{\mathrm{ext}}$ denote prescribed external electric and magnetic fields and $\mathbf{E}_{\mathrm{ext}}$ denotes the retained electric field. Here, the shorter $\mathbf{f}^{\mathrm{mic}}_{\mathrm{L}}$ refers to the selected external-field contribution. We first establish two carrier-to-host transmission rules and then apply them to a controlled pair with the same retained projection of the applied-field carrier loading.

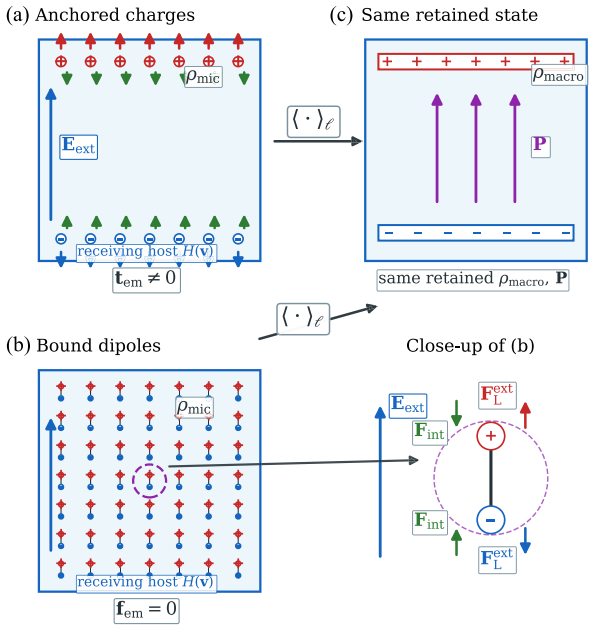


FIG. 1. Carrier-to-host transmission at fixed retained electromagnetic state. The light-blue region is the receiving host $H(\mathbf{v})$; red and blue force arrows show the external-field Lorentz force $\mathbf{F}^{\mathrm{ext}}_{\mathrm{L}}$ on each carrier, and green arrows show support or binding reactions $\mathbf{F}_{\mathrm{int}}$ on the carriers. (a) Individual anchors transmit charge forces locally. (b) A bound constituent carries the end point term internally, so its translational coordinate receives only the dipole resultant. (c) Electromagnetic retention maps the different charge patterns to the same ρ_{macro}, $\mathbf{P}$, and prescribed external field and hence to the same retained applied-field Lorentz projection. The transmission rules act before mechanical retention and give different host loads.

A. Two transmission rules: Anchored charges and bound dipoles

Direct-transfer reference. Panel 1(a) represents separated charges immobilized at material surfaces or interfaces, as in a charged electret. Each charge is tied directly to the selected host $H(\mathbf{v})$ at its anchor. In the quasistatic limit, the anchor reaction transmits the complete microscopic charge-force density locally:

$$\mathbf{f}^{\mathrm{mic}}_{H,\mathrm{anchored}} = \mathbf{f}^{\mathrm{mic}}_{\mathrm{L}} = \rho_{\mathrm{mic}}\mathbf{e}_{\mathrm{ext}}. \tag{26}$$

Thus, in this anchored realization, the stage (2)-to-stage (3) map is direct: the complete Lorentz-force ledger is transmitted to $H(\mathbf{v})$. We next contrast this rule with a mechanically bound dipole, for which the selected host coordinate receives only the dipole resultant.

Bound-dipole contrast. Panel 1(b) represents localized dipoles whose positive and negative end points belong to one mechanically bound constituent. Writing their neutral microscopic charge distribution as $\rho_{\mathrm{mic}} = -\nabla\cdot\mathbf{p}_{\mathrm{mic}}$, a product rule decomposes the same selected carrier ledger as:

$$\mathbf{f}^{\mathrm{mic}}_{\mathrm{L}} = \rho_{\mathrm{mic}}\mathbf{e}_{\mathrm{ext}} = (\mathbf{p}_{\mathrm{mic}}\cdot\nabla)\mathbf{e}_{\mathrm{ext}} - \nabla\cdot(\mathbf{e}_{\mathrm{ext}}\otimes\mathbf{p}_{\mathrm{mic}}). \tag{27}$$

The symbol $\otimes$ denotes a dyadic product, with $(\mathbf{u}\otimes\mathbf{z})_{ij} = u_i z_j$ and $(\nabla\cdot\mathbf{T})_i = \partial_j T_{ij}$ for Cartesian components (summation over j). The product-rule split separates two mechanical actions. The first term is the net force on the bound constituent and is conjugate to translation of the dipole as a whole. Barnett and Loudon show that the dipole form tracks the constituent's center-of-mass force, whereas the charge-resolved form retains the forces on its separated charges [45]. The divergence term can therefore resolve end point forces and internal loading. In the mechanical interpretation adopted here, this internal loading is conjugate to dipole separation or strain. The identity alone does not determine which part loads the selected continuum coordinate; that allocation is supplied by the transmission rule.

Under the bound-translational closure adopted here, each dipole is treated as one material unit, and its internal separation is not retained as an independent mechanical coordinate. The load delivered to $H(\mathbf{v})$ is therefore only the dipole resultant:

$$\mathbf{f}^{\mathrm{mic}}_{H,\mathrm{bound}} = (\mathbf{p}_{\mathrm{mic}}\cdot\nabla)\mathbf{e}_{\mathrm{ext}}. \tag{28}$$

Equations (27) and (28) make the central distinction explicit: under the bound-translational closure, $H(\mathbf{v})$ receives only the net force on each dipole, not the complete end point-force ledger. Thus the microscopic Lorentz-force density need not coincide with the load assigned to

the selected host coordinate even before continuum retention.

B. Controlled result: Equal retained Lorentz projection, different host loads

To expose the role of $\mathcal{C}_T$, we compare two microscopic realizations with the same retained electromagnetic state but different carrier-to-host organization. Panels 1(a) and 1(b) show their distinct charge patterns: anchored charges lie at material surfaces, whereas the bound realization resolves dipole end points throughout the body. Under the retention defined in Sec. III A, the rapidly varying dipole-lattice charge belongs to the microscopic complement; both realizations reduce to the same $\mathbf{P}$, $\rho_{\mathrm{macro}} = -\nabla\cdot\mathbf{P}$, and hence $\mathbf{S}_{\mathrm{EM}}$ shown in panel 1(c). The comparison is therefore controlled at retained, not microscopic, resolution.

To isolate the effect of carrier anchoring, this example considers only the Lorentz-force contribution from the same spatially uniform prescribed external field in both realizations. Internal self- and near-field forces may also affect the body, but they lie outside this controlled comparison. The microscopic charge patterns, and hence the pointwise external-field forces, remain different; because the prescribed field is uniform, their retained projections nevertheless coincide:

$$\begin{aligned}\langle\rho_{\mathrm{mic,anchored}}\rangle_\ell &= \langle\rho_{\mathrm{mic,bound}}\rangle_\ell = \rho_{\mathrm{macro}},\\ \langle\mathbf{f}^{\mathrm{mic}}_{\mathrm{L,anchored}}\rangle_\ell &= \langle\mathbf{f}^{\mathrm{mic}}_{\mathrm{L,bound}}\rangle_\ell = \rho_{\mathrm{macro}}\mathbf{E}_{\mathrm{ext}}.\end{aligned} \tag{29}$$

Thus, if transmission were direct in both realizations, the common continuum-retention rule would give the same host load $\rho_{\mathrm{macro}}\mathbf{E}_{\mathrm{ext}}$.

Instead, $\mathcal{C}_T$ acts on the microscopic force pattern before retention. For the uniform field, Eq. (28) gives $\mathbf{f}^{\mathrm{mic}}_{H,\mathrm{bound}} = \mathbf{0}$, whereas the anchored realization transmits the complete charge-force distribution. Retaining these host loads gives

$$\mathbf{f}^{\mathrm{anchored}}_{\mathrm{em}} = \rho_{\mathrm{macro}}\mathbf{E}_{\mathrm{ext}} = -(\nabla\cdot\mathbf{P})\mathbf{E}_{\mathrm{ext}}, \quad \mathbf{f}^{\mathrm{bound}}_{\mathrm{em}} = \mathbf{0}. \tag{30}$$

Figure 1 makes the distinction local. The anchors in panel (a) pass separated surface forces to $H(\mathbf{v})$, whereas the end point forces in panel (b) close within each dipole; internal dipole stress remains, but the selected translational coordinate receives no load. Denoting these realizations by x_{anchored} and x_{bound}, the witness is therefore:

$$\boxed{\mathbf{S}_{\mathrm{EM}}(x_{\mathrm{anchored}}) = \mathbf{S}_{\mathrm{EM}}(x_{\mathrm{bound}}) = \mathbf{S}_{\mathrm{EM}}, \langle\mathbf{f}^{\mathrm{mic}}_{\mathrm{L,anchored}}\rangle_\ell = \langle\mathbf{f}^{\mathrm{mic}}_{\mathrm{L,bound}}\rangle_\ell, \mathcal{C}_T^{\mathrm{anchored}} \neq \mathcal{C}_T^{\mathrm{bound}}, \mathbf{f}^{\mathrm{anchored}}_{\mathrm{em}} \neq \mathbf{f}^{\mathrm{bound}}_{\mathrm{em}}.} \tag{31}$$

Equation (31) shows that, with the host coordinate and retention rule fixed, the same $\mathbf{S}_{\mathrm{EM}}$ and retained Lorentz projection can yield different local host loads. The missing information is how microscopic carrier forces reach the host: anchors transmit them, whereas bound constituents close them internally. This is a $\mathcal{C}_T$, not a $\mathcal{C}_P$, closure; specifying the relevant transmission topology and support law closes this step.

C. Further transmission limits

The controlled electric witness above showed that the microscopic Lorentz-force ledger need not equal the load transmitted to the selected continuum coordinate. We now consider two further limits—relaxed conduction and bound orbital currents—to show that this distinction is not specific to anchored charges or electric dipoles. These are scope illustrations, not additional nonclosure witnesses.

Relaxed conduction. Conduction carriers are mobile rather than individually anchored, but collisions, contacts, and supports transfer their momentum to the mechanical host. When carrier momentum storage and transport are negligible on the mechanical time scale, the host load approaches the quasistatic direct-transfer limit:

$$\mathbf{f}_{H,c} \simeq \mathbf{f}_{\mathrm{L},c} = \rho_c\mathbf{e}_{\mathrm{ext}} + \mathbf{j}_c\times\mathbf{b}_{\mathrm{ext}}. \tag{32}$$

The subscript c labels conduction carriers: ρ_c and $\mathbf{j}_c$ are their charge and current densities, $\mathbf{f}_{\mathrm{L},c}$ is their external-field Lorentz-force density, and $\mathbf{f}_{H,c}$ is the force density they deliver to the host; microscopic labels are suppressed in this illustration. This direct-transfer limit is conditional: free-carrier status alone need not determine $\mathcal{C}_T$ when carrier momentum storage or transport, contact exchange, pressure, scattering, or drag materially affects transfer to the host.

Bound orbital current. A localized orbital-current dipole provides the magnetic counterpart of the bound electric dipole. Writing $\mathbf{j}^{\mathrm{mic}}_{\mathrm{orb}} = \nabla\times\mathbf{m}_{\mathrm{mic}}$, its Lorentz density in a smooth magnetostatic external field with $\nabla\times\mathbf{b}_{\mathrm{ext}} = \mathbf{0}$ in the dipole region obeys

$$\begin{aligned}\mathbf{j}^{\mathrm{mic}}_{\mathrm{orb}}\times\mathbf{b}_{\mathrm{ext}} &= (\mathbf{m}_{\mathrm{mic}}\cdot\nabla)\mathbf{b}_{\mathrm{ext}}\\ &\quad + \nabla\cdot[\mathbf{m}_{\mathrm{mic}}\otimes\mathbf{b}_{\mathrm{ext}} - (\mathbf{m}_{\mathrm{mic}}\cdot\mathbf{b}_{\mathrm{ext}})\mathbf{I}].\end{aligned} \tag{33}$$

Here $\mathbf{I}$ is the identity tensor. This is the magnetic analogue of Eq. (27) [46]. The first term gives the net translational force on the bound loop, while the divergence term records the pointwise Lorentz-force distribution around it. A rigid bound loop transmits only the net force

and torque to its retained rigid-body coordinates, rather than the complete pointwise carrier ledger.

Together, these limits show that carrier type alone does not determine the continuum load. Direct anchoring or sufficiently relaxed conduction can approach local transfer, whereas bound electric or orbital magnetic dipoles transmit only the generalized loads acting on their retained mechanical modes. These are alternative realizations of $\mathcal{C}_T$, not new nonclosure mechanisms. Having isolated the transmission question, Sec. V fixes $\mathcal{C}_T$ and asks whether deleted microscopic field structure can still change the selected retained load—the $\mathcal{C}_P$ question.

V. MECHANISM II: NEAR-FIELD PROJECTION LOSS

Mechanism II isolates $\mathcal{C}_P$, the second closure question in the four-stage handoff. With carrier-to-host transmission $\mathcal{C}_T$ fixed, it asks whether the retained electromagnetic state $\mathbf{S}_{\mathrm{EM}}$ contains enough information to infer the stage (4) load from a specified stage (3) host-load law. We first identify a closed limit in which retained fields are sufficient and then turn to the unresolved-field case tested by the boundary witness.

For every representative considered below, we fix the same microscopic host-load law,

$$\mathbf{f}_H^{\mathrm{mic}} = (\mathbf{p}_{\mathrm{mic}} \cdot \nabla)\mathbf{e}_{\mathrm{mic}}. \tag{34}$$

Here $\mathbf{e}_{\mathrm{mic}}$ is the regular field acting on the target constituent: the target's own singular self-field is omitted, whereas prescribed fields and the fields of all other constituents, including the body's collective polarization field, are included. Equation (34) fixes the stage (3) load after transmission. Equation (24) defines the stage (4) target: its mesoscopic average gives the retained bulk force density in smooth bulk, while its integral through an unresolved transition layer gives the corresponding sharp-interface traction. The $\mathcal{C}_P$ question is whether that retained load can be evaluated from $\mathbf{S}_{\mathrm{EM}}$ without reconstructing the microscopic source and field.

A. Closed smooth-external-field limit

We begin with the simplest case: the load density generated in a representative element of the bound material by a long-wavelength external field. The microscopic moments are held fixed during the loading increment, and the applied field is smooth across their microscopic support:

$$\begin{aligned}\mathbf{f}_{\mathrm{em,ext}}^{\mathrm{bulk}} &\simeq \langle(\mathbf{p}_{\mathrm{mic}} \cdot \nabla)\mathbf{e}_{\mathrm{ext}}\rangle_{\ell_{\mathrm{mech}}} \\ &= \langle(\mathbf{P} \cdot \nabla)\mathbf{E}_{\mathrm{ext}}\rangle_{\ell_{\mathrm{mech}}} + \langle(\delta\mathbf{p} \cdot \nabla)\mathbf{E}_{\mathrm{ext}}\rangle_{\ell_{\mathrm{mech}}} \\ &\simeq (\mathbf{P} \cdot \nabla)\mathbf{E}_{\mathrm{ext}}, \qquad \delta\mathbf{e}_{\mathrm{ext}} = \mathbf{0}.\end{aligned} \tag{35}$$

Here $\mathbf{f}_{\mathrm{em,ext}}^{\mathrm{bulk}}$ is the retained bulk load from the external field and $\delta\mathbf{e}_{\mathrm{ext}} = \mathbf{e}_{\mathrm{ext}} - \mathbf{E}_{\mathrm{ext}}$ is its microscopic field complement. The last step uses a compatible smooth-bulk averaging plateau for ℓ_{mech}: $\nabla\mathbf{E}_{\mathrm{ext}}$ varies negligibly across the averaging window and $\langle\delta\mathbf{p}\rangle_{\ell_{\mathrm{mech}}} \simeq \mathbf{0}$. Thus the field-first expression gives the retained bulk load from this contribution, and no $\mathcal{C}_P$ data or near-field reconstruction is required. If $\mathbf{E}_{\mathrm{ext}}$ is spatially uniform, this translational dipole load vanishes. The same reasoning applies to a fixed magnetic moment in a field smooth across its microscopic support once the magnetic transmission rule is specified.

B. Projection residual for unresolved fields

Equation (35) established the smooth-field limit: retaining Eq. (34) gives $(\mathbf{P} \cdot \nabla)\mathbf{E}_{\mathrm{ext}}$. We now test whether the same field-first replacement holds for the regular field, including the body's collective self-field and unresolved interconstituent near-field structure. If so, the sharp-profile candidate is

$$\begin{aligned}&\mathbf{f}_{\mathrm{em}}^{\mathrm{bulk}} \stackrel{?}{=} (\mathbf{P} \cdot \nabla)\mathbf{E}, \\ &\mathbf{t}_{\mathrm{em}} \stackrel{?}{=} \mathbf{t}_{\mathrm{fld}}, \\ &\mathbf{t}_{\mathrm{fld}} = \frac{1}{2\epsilon_0}(\hat{\mathbf{n}} \cdot \mathbf{P}_0)^2\hat{\mathbf{n}} \text{ on } \partial\Omega.\end{aligned} \tag{36}$$

Here $\mathbf{t}_{\mathrm{fld}}$ is the self-field reference implied by the field-first construction, not the complete retained traction. The normal Maxwell traction underlying this reference is standard [15,42,44,47]. Writing $\mathbf{E}_{\mathrm{self}}$ for the smooth polarization self-field, this reference is obtained by resolving the polarization-vacuum transition, integrating $(\mathbf{P} \cdot \nabla)\mathbf{E}_{\mathrm{self}}$ across that layer, and taking the sharp-interface limit; for $\mathbf{P} = \mathbf{P}_0\chi_\Omega$, this gives the expression above. We now test whether applying Eq. (24) to Eq. (34) reproduces Eq. (36) or leaves an additional bulk or boundary projection residual.

Using $\mathbf{p}_{\mathrm{mic}} = \mathbf{P} + \delta\mathbf{p}$ and $\mathbf{e}_{\mathrm{mic}} = \mathbf{E} + \delta\mathbf{e}$, the fixed microscopic law becomes

$$\begin{aligned}&\mathbf{f}_H^{\mathrm{mic}} = (\mathbf{P} \cdot \nabla)\mathbf{E} + \mathbf{r}^{\mathrm{mic}}, \\ &\mathbf{r}^{\mathrm{mic}} \equiv (\mathbf{P} \cdot \nabla)\delta\mathbf{e} + (\delta\mathbf{p} \cdot \nabla)\mathbf{E} + (\delta\mathbf{p} \cdot \nabla)\delta\mathbf{e}.\end{aligned} \tag{37}$$

The vector $\mathbf{r}^{\mathrm{mic}}$ is the microscopic force-density residual relative to the field-first term. Equation (37) is still a microscopic statement. Applying Eq. (24) gives, relative to the field-first candidate in Eq. (36),

$$\begin{aligned}\mathbf{f}_{\mathrm{em}}^{\mathrm{bulk}} &\simeq (\mathbf{P} \cdot \nabla)\mathbf{E} + \Delta\mathbf{f}_{\mathrm{bulk}}, \\ \Delta\mathbf{f}_{\mathrm{bulk}} &\equiv \langle\mathbf{r}^{\mathrm{mic}}\rangle_{\ell_{\mathrm{mech}}}, \\ \mathbf{t}_{\mathrm{em}} &\simeq \mathbf{t}_{\mathrm{fld}} + \Delta\mathbf{t}_{\partial\Omega}, \\ \Delta\mathbf{t}_{\partial\Omega} &\equiv \int_{\text{unresolved layer}} \mathbf{r}^{\mathrm{mic}}\, dn.\end{aligned} \tag{38}$$

In smooth bulk, under the scale separation and on the averaging plateau established in Sec. III A, the mixed

low-high terms average away,

$$\langle(\mathbf{P}\cdot\nabla)\delta\mathbf{e}\rangle_{\ell_{\mathrm{mech}}}\simeq 0, \qquad \langle(\delta\mathbf{p}\cdot\nabla)\mathbf{E}\rangle_{\ell_{\mathrm{mech}}}\simeq 0.$$

The high-high correlation need not vanish, however, because its product can contain a retained low-frequency component. Hence

$$\Delta\mathbf{f}_{\mathrm{bulk}}\simeq\langle(\delta\mathbf{p}\cdot\nabla)\delta\mathbf{e}\rangle_{\ell_{\mathrm{mech}}}$$

can remain nonzero even on the smooth-bulk averaging plateau.

At a sharp interface, however, the position-insensitive averaging plateau described in Sec. III A generally does not exist. Even the mixed low-high terms in Eq. (37) can therefore survive the unresolved-layer integral in Eq. (24). The field-first expressions consequently provide a candidate bulk load and a retained self-field reference traction but not the complete continuum load in general.

Microstructure-dependent near-boundary fields, surface energetics, and loading are well established in particle-resolved and atomistically informed multiscale descriptions [22,24,33]. Enriched Helmholtz formulations represent such dependence through electrostrictive or magnetostrictive coefficients [23,34,35]. These approaches show that microscopic structure can enter the continuum load through explicit multiresolution reconstruction, surface-energy variations, or enriched constitutive data.

Our purpose here is narrower and complementary: Eqs. (37) and (38) locate where this information is lost in the stage (3)-to-stage (4) handoff. Retaining $\mathbf{P}$ and $\mathbf{E}$ separately deletes $\delta\mathbf{p}$ and $\delta\mathbf{e}$ before the microscopic source-field product is formed. The terms thereby omitted from the field-first expression can nevertheless survive continuum retention as a bulk load or boundary traction. This mechanically retained projection residual, or an output-equivalent representation of it, is what projection closure $\mathcal{C}_P$ must represent. The next subsection and Fig. 2 make this need explicit through a controlled comparison of two boundary realizations with the same retained state and transmission closure but different retained tractions.

C. Controlled equal-state boundary witness

To isolate $\mathcal{C}_P$, we construct aligned and staggered realizations with the same retained electromagnetic state $\mathbf{S}_{\mathrm{EM}}$, in particular the same $\mathbf{P}$ and $\mathbf{E}$, and the same transmission closure $\mathcal{C}_T$, but different deleted microscopic registry and its boundary termination. The continuum body, electromagnetic boundary data, mechanical resolution, host-load law in Eq. (34), and sharp-interface convention are also fixed. If the field-first candidate in Eq. (36) were complete, these equal-retained data would imply equal continuum loads. We show instead that the retained boundary corrections, and hence the tractions, differ.

Each two-dimensional constituent i is a line dipole $\mathbf{p}_i = p_0\hat{\mathbf{y}}$, where $\hat{\mathbf{y}}$ is the unit vector along y and p_0 is dipole moment per unit out-of-plane length (SI unit C). Let

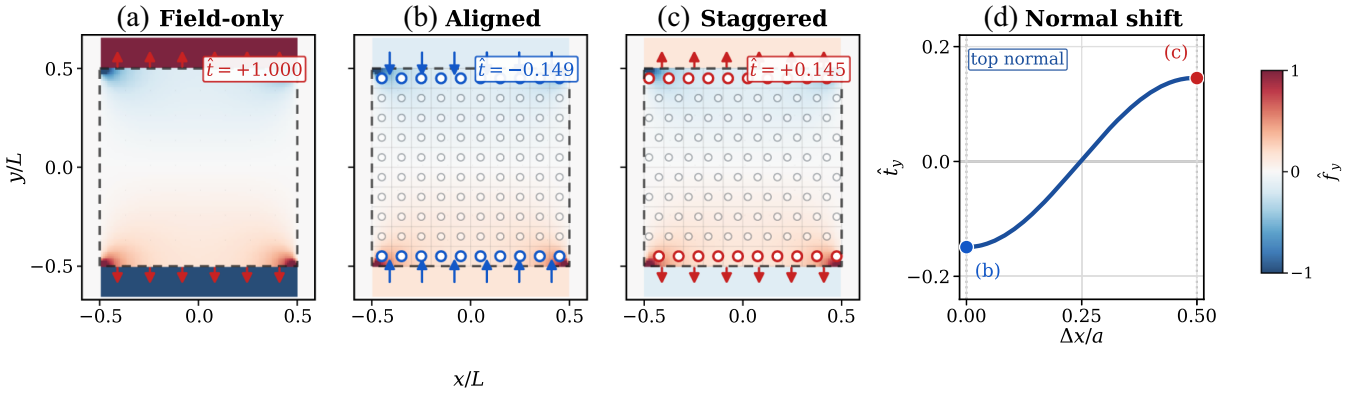


FIG. 2. Controlled stage (3)-to-stage (4) localization witness within the matched line-dipole benchmark, at fixed $\mathbf{S}_{\mathrm{EM}}$ and $\mathcal{C}_T$. Panels (a)–(c) use macroscopic coordinates x/L and y/L, where L is the body width. The dipole markers schematically indicate the local registry and are not to scale; they do not represent the number of dipoles in the body or the cavity size. The end point corrections in panels (b) and (c) are the $N = 15$ matched-cavity estimates, with larger-window checks in Appendix. Panel (d) is an end point-anchored local-neighborhood trace versus the relative lateral row shift $\Delta x/a$. (a) The common field-first continuum force density gives the tensile normalized top-traction resultant $\hat{t} = +1.00$. (b) Restoring the aligned neighborhood gives $\hat{t} \simeq -0.149$. (c) Restoring the row-staggered neighborhood gives $\hat{t} \simeq +0.145$. (d) The trace illustrates continuous registry sensitivity; intermediate values are not full cavity reconstructions. The retained state and transmission remain fixed. The numerical values characterize this benchmark; the controlled conclusion is the top-traction difference under equal-retained data. The color scale is $\hat{f}_y = h_{\mathrm{vis}} f_y^{\mathrm{vis}}/t_{\mathrm{fld}}$, where f_y^{vis} is the displayed y-directed force density and $h_{\mathrm{vis}} = 0.15L$ is the display-layer thickness used to spread each surface traction for visualization. It is not a physical interface thickness. The ordinate $\hat{t}_y$ in panel (d) is the normalized top traction $\hat{t}$ of Eq. (41). Computational assistance is disclosed in Appendix.

a be the lattice spacing. The aligned lattice has vertically registered rows; in the staggered lattice, alternating rows shift by $\pm a/4$, giving a row-to-row offset $a/2$. Under the retention defined in Sec. III A, this $O(a)$ shift lies outside the retained bulk band because $a \ll \ell$. At the boundary, we impose the same sharp-interface profile $\mathbf{P}_0\chi_\Omega$, with Ω fixed independently of the outermost dipoles. Hence

$$\langle \mathbf{p}^s_{\mathrm{mic}} \rangle_\ell = \mathbf{P}_0 = \frac{p_0}{a^2}\hat{\mathbf{y}}, \quad s \in \{\mathrm{al}, \mathrm{st}\}, \quad \mathbf{P}(\mathbf{x}) = \mathbf{P}_0\chi_\Omega(\mathbf{x}). \tag{39}$$

The label $s = $ al or st identifies the aligned or staggered registry. The registry shift therefore changes only the deleted polarization complement $\delta\mathbf{p}^s$, its associated near-field complement $\delta\mathbf{e}^s$, and the unresolved boundary termination—precisely the microscopic quantities entering $\mathbf{r}^{\mathrm{mic}}$ in Eq. (37). The retained state $\mathbf{S}_{\mathrm{EM}}$ remains the same in smooth bulk and at the prescribed sharp boundary. At fixed $\mathbf{P}_0$, a only sets the representative microscopic scale; Appendix verifies scale covariance of the normalized benchmark.

To reconstruct the omitted near-field contribution without resolving every dipole in the macroscopic body, we use a matched multiresolution cavity. The common far field remains at continuum resolution. Around a representative boundary site, a finite smooth neighborhood is replaced by the actual dipoles of each registry. At each cavity size, the correction is the force from the actual dipoles minus the force of the matched smooth neighborhood. The cavity is enlarged until the accumulated correction converges, after which the result is averaged along the macroscopic boundary. Classical local-field cavity decompositions are established [42,44,48], while related atomistic-continuum and long-range electrostatic coupling frameworks provide fine and coarse, overlap, and subtraction ingredients [21,22,49,50]. The specific actual-minus-smooth boundary reconstruction used here is our diagnostic implementation. Appendix gives the exact matched subtraction, convergence tests, and scale-covariance check. Bulk symmetry cancels the correction, whereas boundary termination leaves

$$\mathbf{t}_{\mathrm{em}} = \mathbf{t}_{\mathrm{fld}} + \Delta\mathbf{t}, \qquad \Delta\mathbf{t} = \langle \Sigma \Delta\mathbf{F}_{\mathrm{cavity}} \rangle_S. \tag{40}$$

Here $\Delta\mathbf{F}_{\mathrm{cavity}}$ is the actual-minus-smooth local force defect defined in Eq. (A2), Σ accumulates defects through the boundary layer, and $\langle\cdot\rangle_S$ performs the surface averaging and normalization specified in Eq. (A4). For the benchmark below, $\Delta\mathbf{t} \equiv \Delta\mathbf{t}_{\partial\Omega}$ in Eq. (38).

For comparison with the common field-first baseline shown in Fig. 2(a), define

$$\hat{t} = \frac{t_y}{t_{\mathrm{fld}}}, \qquad \widehat{\Delta t} = \frac{\Delta t_y}{t_{\mathrm{fld}}}. \tag{41}$$

Here $t_y = \mathbf{t}_{\mathrm{em}} \cdot \hat{\mathbf{y}}$ and $\Delta t_y = \Delta\mathbf{t} \cdot \hat{\mathbf{y}}$ are the top-boundary components, and $t_{\mathrm{fld}} = \mathbf{t}_{\mathrm{fld}} \cdot \hat{\mathbf{y}} > 0$ is their common outward self-field reference from Eq. (36).

Let x_{al} and x_{st} denote the aligned and staggered representatives. The controlled result is

$$\boxed{\mathbf{S}_{\mathrm{EM}}(x_{\mathrm{al}}) = \mathbf{S}_{\mathrm{EM}}(x_{\mathrm{st}}) = \mathbf{S}_{\mathrm{EM}}, \quad \mathcal{C}_T^{\mathrm{al}} = \mathcal{C}_T^{\mathrm{st}}, \quad \mathbf{t}_{\mathrm{em}}^{\mathrm{al}} \neq \mathbf{t}_{\mathrm{em}}^{\mathrm{st}}.} \tag{42}$$

Because the retained inputs and $\mathcal{C}_T$ are fixed by construction, the unequal tractions in Eq. (42) isolate $\mathcal{C}_P$. The missing information is the boundary registry and termination, or an equivalent reduced correction not contained in $\mathbf{S}_{\mathrm{EM}}$.

Figure 2 gives the quantitative witness. The common self-field baseline is $\hat{t} = +1.00$. Restoring the aligned neighborhood gives $\widehat{\Delta t} \simeq -1.149$ and $\hat{t} \simeq -0.149$, whereas the staggered neighborhood gives $\widehat{\Delta t} \simeq -0.855$ and $\hat{t} \simeq +0.145$. The sign change follows from the near-field gradient sampled by a boundary dipole: an aligned top dipole lies above a direct neighbor and receives a strong inward correction, whereas staggering replaces that neighbor with two diagonal neighbors and weakens the correction. Distant dipoles produce the common smooth field, the interior defect vanishes in the large-window limit, and boundary termination leaves the retained traction. The end point-anchored local trace in Fig. 2(d) illustrates continuous registry sensitivity.

The difference is the retained contribution of $\mathbf{r}^{\mathrm{mic}}$ in Eq. (37), which is omitted by the field-first projection but whose unresolved-layer integral survives the retention rule in Eq. (24). Because a sharp interface has no unique spectral split, the cavity reconstruction determines the total $\Delta\mathbf{t}$ without assigning it uniquely to any individual term in $\mathbf{r}^{\mathrm{mic}}$.

Pressure-to-tension reversals caused by microscopic lattice structure or symmetry have been reported previously [24]. Related microstructure-dependent contributions can also appear as bulk or internal force densities when symmetry does not cancel them [23,51]. The contribution here is the controlled localization of the boundary-traction difference in a fixed-dipole equal-state pair and the identification of the missing information with $\mathcal{C}_P$.

If the residual affects the selected output above the target accuracy, $\mathcal{C}_P$ must be supplied through structural data, a reduced correction, multiresolution reconstruction, or a validated enriched macroscopic law; if it is negligible, the validated macroscopic load law remains sufficient. Section VI develops this audit and the available closure routes.

VI. WHEN CLOSURE IS NEEDED AND HOW TO SUPPLY IT

Section s IV and V identify two ordered closure problems: carrier-to-host transmission $\mathcal{C}_T$ and projection closure $\mathcal{C}_P$. This section turns that distinction into an output-first closure audit and summarizes how either unresolved closure can be supplied.

A. Output-first closure audit

The audit stops as soon as the selected output is closed:

(1) Declare the receiving system or host $H(\mathbf{v})$, the requested mechanical output, its resolution, and the target accuracy. If a global balance already fixes the requested total force or torque on that receiving system, no local closure is needed. A force on a selected constituent or subsystem may still require the following steps.

(2) If localization is required, establish how the active carrier loading reaches the host, thereby fixing $\mathcal{C}_T$. If that transmission is output-relevant but unresolved, a material-support, momentum-transfer, or carrier-kinetic model must be supplied; finer electromagnetic resolution alone cannot determine the host load.

(3) With $\mathcal{C}_T$ fixed or irrelevant, use Eq. (24) to test whether electromagnetic retention deletes source-field structure whose retained bulk or surface contribution changes the selected output above the target tolerance. If not, the validated macroscopic load law is sufficient. If it does, supply $\mathcal{C}_P$.

Three cases make the projection audit concrete. (i) The retained bulk residual vanishes for fixed microscopic moments in a prescribed external field that is smooth across their support: Eq. (35) gives $(\mathbf{P}\cdot\nabla)\mathbf{E}_{\mathrm{ext}}$, and no $\mathcal{C}_P$ is required. (ii) A residual may exist, but the audit still stops if symmetry cancels it, the selected observable integrates it out, or it lies below the target tolerance. (iii) $\mathcal{C}_P$ is required only when unresolved source-field correlations—such as a polarization self-field at a sharp interface or an imposed near field varying on the microscopic scale—survive the retention in Eq. (24) and change the retained bulk force density or traction above that tolerance. Field origin is therefore not the criterion.

B. Supplying the missing closure

Only after the audit identifies an unresolved closure is a closure route required. A failed $\mathcal{C}_T$ calls for the relevant support, carrier kinetics, or momentum-transfer path; a failed $\mathcal{C}_P$ calls for the relevant source-field correlation, registry, termination, near-field neighborhood, or an output-equivalent reduced correction. The diagnostic identifies these requirements; a material model or measurements must supply the corresponding closure data. The following three route families are a practical synthesis of established approaches and may be combined.

1. Direct multiresolution reconstruction. Scale separation often permits a representative bulk or interface cell rather than resolution of the entire body. Established atomistic-continuum coupling methods supply fine and coarse partitions, matched or overlapping regions, subtraction rules that avoid double counting, and cell-size convergence tests [49,50]. Electromechanical and long-range electrostatic extensions treat field-mediated interactions [21,22], while particle-resolved force-density calculations provide related local benchmarks [25]. Appendix illustrates one implementation for $\mathcal{C}_P$: it fixes the retained state and $\mathcal{C}_T$; reconstructs only the deleted boundary neighborhood; and tests convergence, bulk cancellation, registry dependence, and scale covariance. These checks establish consistency within the prescribed microscopic model; validation for a specific real material remains open. Analogously, direct reconstruction can supply $\mathcal{C}_T$ when the resolved model includes carrier collisions, contacts, supports, and momentum exchange.

2. Energy or constitutive closure. A deformation-dependent free energy, stress law, or enriched continuum model can encode the output-relevant effect of deleted structure without reconstructing that structure explicitly. Classical and finite-deformation electroelasticity provide established examples [8,10,14–18,20]; magneto-electroelastic, electrostrictive, magnetostrictive, and switching models illustrate how additional constitutive variables or evolution laws enter [11–13,19,52,53]. For $\mathcal{C}_P$, the chosen state must encode both the unresolved contribution and how it changes under the retained deformation; relations such as $\mathbf{D}(\mathbf{E})$, $\mathbf{P}(\mathbf{E})$, or $\mathbf{M}(\mathbf{H})$ alone need not suffice. A specified free energy closes only its stated reversible material class; dissipative, hysteretic, switching, or evolving systems also require the corresponding history and evolution laws.

3. Experimental or inverse closure. When microscopic structure is inaccessible, measured force, deformation, displacement, or modal response can be combined with a forward mechanical model to identify an effective traction or stress law and its parameters. Drop-deformation experiments [4,54], optical bulk and surface-force measurements [3], and solid electromechanical or optomechanical tests [1,2] provide relevant observables; broader experimental comparisons of electromagnetic force models are given in Refs. [26,27]. Such data generally identify only the combined state-to-load map, not $\mathcal{C}_T$ and $\mathcal{C}_P$ separately. The resulting closure is therefore limited to the stated material, geometry, loading range, mechanical model, and output, and should be validated under independent loading paths or geometries.

The routes may also form a sequence: local reconstruction can generate a reduced constitutive correction, and experiments can calibrate or validate it. A

material-specific test would compare predictions from a chosen macroscopic load model before and after supplying the identified closure information. Independent measurements or a separately validated microscopic calculation would provide the reference for the same mechanical observable. The least demanding validated route, or combination of routes, that closes the selected output is sufficient. The audit therefore does not rank named force or stress expressions; it asks whether a chosen law, together with its recipient, transmission, interface, and retention assumptions, fixes or renders irrelevant $\mathcal{C}_T$ and $\mathcal{C}_P$ for the declared material, resolution, and output.

VII. CONCLUSION

We developed an output-first diagnostic for deciding whether a retained electromagnetic description supplies the local load required for a declared receiving system, mechanical output, resolution, and tolerance. The four-stage handoff first identifies the selected carrier Lorentz-force ledger and receiving host $H(\mathbf{v})$. Once the reference model, selected ledger and host, declared output, and continuum-retention convention are fixed, it factorizes any remaining closure need into the ordered, noninterchangeable stage (2)-to-stage (3) transmission question $\mathcal{C}_T$ and, after transmission and the microscopic host-load law are fixed, the stage (3)-to-stage (4) projection question $\mathcal{C}_P$. This factorization is conditionally exhaustive for missing closure in the declared handoff; reference model, constitutive, and numerical errors lie outside that classification. The ordering has an operational consequence: electromagnetic refinement cannot determine an unspecified transmission map, whereas fixing transmission cannot recover source-field structure deleted before the local load is formed.

Two controlled equal-state witnesses isolate these questions. Mechanism I fixes the retained electromagnetic state and retained projection of the prescribed-field carrier loading while changing support topology; the resulting host-load difference isolates $\mathcal{C}_T$. Mechanism II fixes $\mathcal{C}_T$, the retained fields, continuum body, and microscopic host-load law while changing the deleted microscopic registry, whose bulk contribution cancels but whose boundary termination produces different retained tractions; this difference isolates $\mathcal{C}_P$. The source-field expansion localizes the projection residual and distinguishes smooth-bulk averaging from unresolved-interface retention, while the matched actual-minus-smooth reconstruction verifies convergence, bulk cancellation, and scale covariance within the line-dipole benchmark. These are structural nonuniqueness results within the declared comparison classes; the reported tractions are not universal material predictions.

The resulting minimum-closure audit stops if global balance fixes the requested total force or torque. If localization remains necessary, it establishes $\mathcal{C}_T$ before testing whether deleted source-field structure leaves a bulk or surface residual that affects the selected output above tolerance. For fixed microscopic moments in a prescribed field smooth across their support, the external-field contribution is already closed; other residuals may cancel by symmetry, be integrated out by the observable, or fall below tolerance. An unresolved $\mathcal{C}_T$ requires support, momentum-transfer, or carrier-kinetic information, whereas an unresolved $\mathcal{C}_P$ requires the relevant source-field correlation or an output-equivalent correction supplied through reconstruction, a constitutive model, or inverse calibration. For the declared material class and task, a validated macroscopic load law is sufficient whenever transmission is fixed or irrelevant and every output-relevant residual is negligible or already represented.

ACKNOWLEDGMENTS

Open-access publication of this article was supported by Technische Universität Berlin under its read-and-publish agreement with the American Physical Society.

DATA AVAILABILITY

Code and numerical data supporting the line-dipole benchmark, including its reported numerical values and figures, are publicly archived on Zenodo in Ref. [55]. The version-specific archive contains Python scripts, automated tests, generated figure data, and instructions for reproducing the reported results. The Zenodo record is cited in the manuscript.

APPENDIX: LOCAL-CAVITY RECONSTRUCTION PROTOCOL AND BOUNDARY CONVERGENCE

Purpose and scope. This appendix reconstructs the traction defect in Fig. 2 at the fixed retained state, transmission, host-load law, and interface convention specified in Sec. V. Scale separation permits the common far field to remain at continuum resolution while a finite, registry-sensitive neighborhood is restored and enlarged to convergence. Classical electromagnetic cavity decompositions [42,44,48] and related atomistic-continuum coupling methods [21,22,49,50] provide the background. Their combination here reconstructs the stage (4) traction defect; it is not an independent force law or a simulation of the complete microscopic body.

Matched replacement. The retained body Ω and its smooth continuum grid are fixed first, independently of microscopic row shifts, with one continuum cell matched to one line dipole. The smooth model assigns $(\mathbf{P}\cdot\nabla)\mathbf{E}$ and the common sharp-interface traction; the microscopic model assigns $(\mathbf{p}_i\cdot\nabla)\mathbf{e}$ to target dipole i, with $\mathbf{e}$ denoting the regular microscopic field acting on that target. For each target, Fig. 3 keeps the full smooth load, subtracts the smooth contribution of an $N\times N$ target-plus-buffer

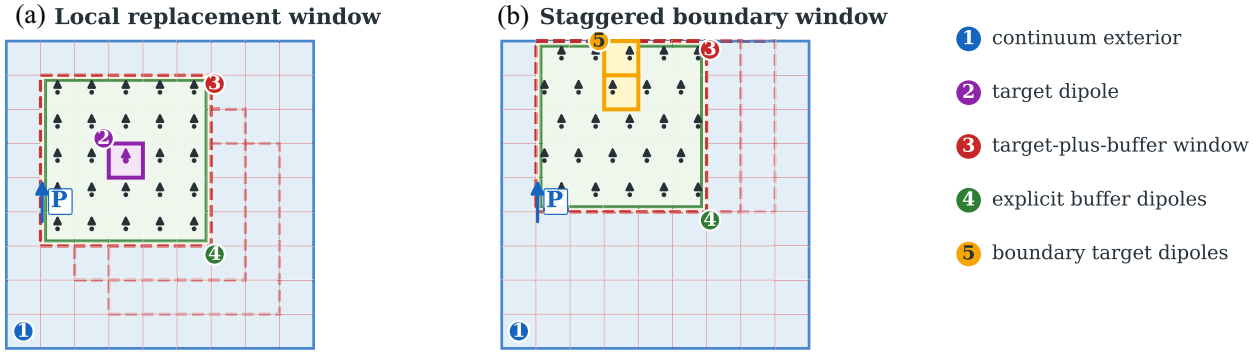


FIG. 3. Matched continuum-dipole replacement. The blue grid is the common continuum envelope, with one cell per line dipole. (a) Aligned interior target and translated target-plus-buffer windows. (b) Staggered 5×5 boundary window; yellow reference cells are accumulated through the boundary layer, while their dipoles shift inside them. In each window, the smooth contribution is subtracted, actual dipoles are inserted, and the target self term is omitted. Computational assistance is disclosed in Appendix.

window (N cells along each direction), and inserts the actual dipoles in that window. The target self term is omitted. Only this neighborhood is resolved microscopically; the exterior remains the same continuum far field for both registries. This fixed envelope isolates the registry: if the boundary were instead defined by the outermost dipoles, shifting the rows would also change the retained geometry and polarization profile, so any load difference could reflect a different macroscopic body rather than the unresolved boundary registry.

For target cell i, the matched reference load is

$$\mathbf{F}_i^{\mathrm{ref}}(N) = \underbrace{\mathbf{F}_{i,\mathrm{cont,full}} - \mathbf{F}_{i,\mathrm{cont,cavity}}(N)}_{\text{continuum far field}} + \underbrace{\mathbf{F}_{i,\mathrm{disc,cavity}}(N)}_{\text{discrete near field}}. \tag{A1}$$

Here $\mathbf{F}_{i,\mathrm{cont,full}}$ is the full smooth cell load, $\mathbf{F}_{i,\mathrm{cont,cavity}}$ is its contribution from the local window, and $\mathbf{F}_{i,\mathrm{disc,cavity}}$ is the force from the actual dipoles in that window. The first two terms retain the common continuum exterior; the last restores the deleted neighborhood. Relative to the full smooth cell load, the local defect is therefore,

$$\Delta\mathbf{F}_i(N) = \mathbf{F}_{i,\mathrm{disc,cavity}}(N) - \mathbf{F}_{i,\mathrm{cont,cavity}}(N). \tag{A2}$$

At finite N, Eq. (A2) is the actual neighborhood minus the smooth neighborhood it replaces. Its converged boundary sum reconstructs Eq. (38). Because a sharp interface has no cutoff-independent spectral gap, the total correction cannot be assigned uniquely to the high-high term in Eq. (37); mixed low-high terms may also contribute. Both continuum terms use the same cell envelope and polarization magnitude $P = |\mathbf{P}_0| = p_0/a^2$: $(\mathbf{P}\cdot\nabla)\mathbf{E}$ is integrated over matched bulk cells, and $(\hat{\mathbf{n}}\cdot\mathbf{P})^2/(2\epsilon_0)$ is assigned to top and bottom boundary cells.

Line-dipole force model. The microscopic input $\mathbf{F}_{i,\mathrm{disc,cavity}}$ uses the same two-dimensional pair law in both registries. All dipoles are $p_0\hat{\mathbf{y}}$, and forces are per unit out-of-plane length. For target i and source j, let $\Delta x = x_i - x_j$, $\Delta y = y_i - y_j$, and $r^2 = \Delta x^2 + \Delta y^2$. With $\mathbf{e}_j$ being the field of source j evaluated at target i, applying $\mathbf{F}_{ij} = (\mathbf{p}_i\cdot\nabla)\mathbf{e}_j = p_0\partial_{\Delta y}\mathbf{e}_j$ to the line-dipole field gives

$$\mathbf{F}_{ij} = \frac{p_0^2}{2\pi\epsilon_0}\left(\frac{2\Delta x(\Delta x^2 - 3\Delta y^2)}{r^6}, \frac{2\Delta y(3\Delta x^2 - \Delta y^2)}{r^6}\right), \qquad j \neq i. \tag{A3}$$

Thus $\mathbf{F}_{i,\mathrm{disc,cavity}}(N) = \sum_{j\in C_i(N), j\neq i}\mathbf{F}_{ij}$, where $C_i(N)$ is the set of dipoles in the $N \times N$ window. The self term is omitted. Only the neighbor separations change between registries.

Boundary accumulation and convergence. The odd window size N is a convergence parameter, not a material parameter: increasing it restores more of the deleted neighborhood while leaving the continuum exterior fixed. For each N, translationally equivalent targets share one defect, so only inequivalent environments are evaluated. The aligned lattice has five classes—bulk, top, bottom, left, and right—while the staggered lattice has seven because each side termination splits into two classes.

An interior window has one central target [Fig. 3(a)]. At a flat boundary, one representative normal column contains $(N-1)/2$ boundary-layer targets [Fig. 3(b)]. They share a surface-anchored window, with the remaining cells providing the buffer; increasing N enlarges both the target layer and the buffer, and convergence is checked on their accumulated defect. For a boundary segment S, let $\mathcal{B}_S$ contain all boundary-layer target indices in one periodic repeat of tangential length L_S. Then the surface homogenization in Eq. (40) is

$$\Delta\mathbf{t}_S(N) = \frac{1}{L_S}\sum_{i\in\mathcal{B}_S}\Delta\mathbf{F}_i(N). \tag{A4}$$

Here $\Delta\mathbf{t}_S(N)$ is the traction correction for that repeat at window size N. For top and bottom, $L_S = a$; the staggered

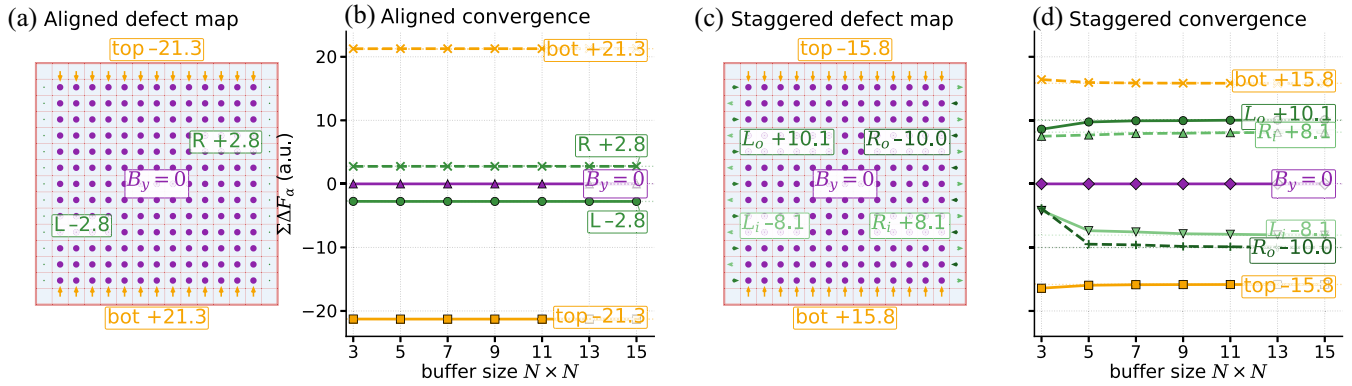


FIG. 4. Panels (a) and (b) show the aligned registry; panels (c) and (d) show the staggered registry. Local-cavity convergence for the two registries. (a),(c) Accumulated $N = 15$ boundary defects mapped to representative boundary cells; purple denotes bulk, yellow denotes top and bottom, and green denotes side terminations. (b),(d) Signed accumulated component $\Sigma\Delta F_\alpha$ versus N, with $\alpha = y$ for top and bottom and $\alpha = x$ for sides; a.u. denotes the common calculation units used for $T_{\rm fld}$ in Eq. (A5). The bulk curve B_y is the central vertical component; the horizontal finite-window residual is documented in the reproduction package. Boundary corrections differ between registries. Computational assistance is disclosed in Appendix.

side classes repeat over $2a$. In Fig. 4, L_o, L_i, R_o, R_i denote outward- and inward-shifted classes at the left and right boundaries. For the representative top column, $T_{\rm fld} = t_{\rm fld} a$.

We plot $N = 3, 5, \ldots, 15$ and check larger windows through $N = 61$. Both registries use identical continuum cell integrals and Eq. (A3); the common exterior cancels from the defect. Increasing N from 15 to 61 changes the staggered normalized top traction by less than 6×10^{-4} and the aligned value by less than 8×10^{-8}. The sign contrast is stable; staggered side classes converge more slowly and are retained as diagnostics. The plotted central vertical component B_y vanishes to numerical precision; the staggered finite-window horizontal residual decreases toward zero. Independent quadrature, full-vector bulk, and rectangular-window checks are provided in the reproduction package. The r^{-3} pair-force tail is absolutely convergent for a fixed target; convergence of accumulated boundary sums is assessed separately for the tested window families.

Normalization and scale covariance. Let $T_{\rm fld}$ be the common retained self-field top traction integrated over the representative surface column. Adding the converged defect gives

$$\hat{t}_{\rm top} = 1 + \frac{\Sigma\Delta F_{\rm top}}{T_{\rm fld}}. \tag{A5}$$

Here $\Sigma\Delta F_{\rm top}$ is the summed y-component of the defects in the representative top column, and $\hat{t}_{\rm top}$ is the $\hat{t}$ of Eq. (41). With $a = 0.3$, $p_0 = 1$, and $\epsilon_0 = 1$ in calculation units, we use the exact normalization $T_{\rm fld} = p_0^2/(2\epsilon_0 a^3)$. For $N = 15$, the aligned and staggered top defects are approximately -21.28 and -15.83, yielding normalized top tractions $\hat{t}_{\rm top} \simeq -0.149$ and $+0.145$, respectively.

The field-only side traction is zero, so no side baseline normalization is used. The class-resolved lateral defects in Fig. 4(c,d) are retained as convergence diagnostics; the main witness and the quoted normalized values use the top-normal traction.

Registry-shift trace. Here Δx denotes the relative lateral shift between neighboring rows. The end point values at $\Delta x/a = 0$ and $1/2$ in Fig. 2(d) are the $N = 15$ cavity estimates checked above. At intermediate shifts, the plotted curve evaluates the vertical force on a boundary target from a three-row, 14-neighbor stencil and maps this continuous local signal to the two end point tractions. It therefore illustrates continuous local registry sensitivity, rather than a full cavity reconstruction at every intermediate shift.

Under a uniform rescaling of the idealized line-dipole lattice at fixed retained $\mathbf{P}$, $p_0 = |\mathbf{P}|a^2$. Writing F_{ij}, ΔF, and Δt for the corresponding force and traction magnitudes, the pair force and boundary traction then scale as:

$$F_{ij} \sim \frac{p_0^2}{\epsilon_0 a^3} \sim \frac{|\mathbf{P}|^2 a}{\epsilon_0}, \qquad \Delta t \sim \frac{\Delta F}{a} \sim \frac{|\mathbf{P}|^2}{\epsilon_0} \sim t_{\rm fld}.$$

Thus $\Delta t/t_{\rm fld}$ is independent of a. Together, buffer convergence, bulk cancellation, the converged end point contrast, and scale covariance support this fixed-dipole benchmark internally, not as an algorithm-independent or material-specific prediction. Other source models require their own closure and validation.

Computational assistance. At the author's direction, OpenAI Codex (GPT-6) assisted with the code audit, validation scripts, figure revisions, and associated methodological text. The resulting calculations were checked against pair-energy derivatives, independent quadrature, symmetry, and convergence controls recorded in the reproduction package.

[1] X. Xi, J. Ma, Z.-H. Zhou, X.-X. Hu, Y. Chen, C.-L. Zou, C.-H. Dong, and X. Sun, Experimental investigation of the angular symmetry of optical force in a solid dielectric, Optica **8**, 1435 (2021).

[2] M. Wang, S. Wang, Q. Zhang, C. T. Chan, and H. B. Chan, Measurement of mechanical deformations induced by enhanced electromagnetic stress on a parallel metallic-plate system, Phys. Rev. Lett. **121**, 035502 (2018).

[3] N. G. C. Astrath, G. A. S. Flizikowski, B. Anghinoni, L. C. Malacarne, M. L. Baesso, T. Požar, M. Partanen, I. Brevik, D. Razansky, and S. E. Bialkowski, Unveiling bulk and surface radiation forces in a dielectric liquid, Light: Sci. Appl. **11**, 103 (2022).

[4] O. Vizika and D. A. Saville, The electrohydrodynamic deformation of drops suspended in liquids in steady and oscillatory electric fields, J. Fluid Mech. **239**, 1 (1992).

[5] A. Ricoeur and M. Kuna, Electrostatic tractions at dielectric interfaces and their implication for crack boundary conditions, Mech. Res. Commun. **36**, 330 (2009).

[6] Y. Wan, L. Fan, and Z. Zhong, Finite element modeling of temporal evolution of the quasi-piezoelectric d_{33} coefficient of cellular piezoelectret polypropylene film, Comput. Mater. Sci. **55**, 54 (2012).

[7] M. Torbati, K. Mozaffari, L. Liu, and P. Sharma, Coupling of mechanical deformation and electromagnetic fields in biological cells, Rev. Mod. Phys. **94**, 025003 (2022).

[8] Z. Suo, X. Zhao, and W. H. Greene, A nonlinear field theory of deformable dielectrics, J. Mech. Phys. Solids **56**, 467 (2008).

[9] Y. M. Shkel, Electrostriction: Material parameters and stress/strain constitutive relations, Philos. Mag. **87**, 1743 (2007).

[10] X. Zhao and Z. Suo, Theory of dielectric elastomers capable of giant deformation of actuation, Phys. Rev. Lett. **104**, 178302 (2010).

[11] A. R. Balakrishna, J. E. Huber, and C. M. Landis, Nanoactuator concepts based on ferroelectric switching, Smart Mater. Struct. **23**, 085016 (2014).

[12] L. Daniel, O. Hubert, N. Buiron, and R. Billardon, Reversible magneto-elastic behavior: A multiscale approach, J. Mech. Phys. Solids **56**, 1018 (2008).

[13] Z. Cao and J. Cai, Design of a giant magnetostrictive motor driven by elliptical motion, Sens. Actuat. A **118**, 332 (2005).

[14] R. Toupin, The elastic dielectric, J. Ration. Mech. Anal. **5**, 849 (1956).

[15] L. D. Landau and E. M. Lifshitz, Electrodynamics of continuous media, in *Course of Theoretical Physics*, edited by E. M. Lifshitz and L. P. Pitaevskii, 2nd ed. (Pergamon Press, Oxford, 1984), Vol. 8.

[16] H. A. Haus and J. R. Melcher, *Electromagnetic Fields and Energy* (Prentice Hall, Englewood Cliffs, NJ, 1989).

[17] J. R. Melcher, *Continuum Electromechanics* (MIT Press, Cambridge, MA, 1981).

[18] R. M. McMeeking and C. M. Landis, Electrostatic forces and stored energy for deformable dielectric materials, J. Appl. Mech. **72**, 581 (2005).

[19] L. Liu, An energy formulation of continuum magneto-electro-elasticity with applications, J. Mech. Phys. Solids **63**, 451 (2014).

[20] L. Dorfmann and R. W. Ogden, Nonlinear electroelasticity: Material properties, continuum theory and applications, Proc. R. Soc. A **473**, 20170311 (2017).

[21] J. Marshall and K. Dayal, Atomistic-to-continuum multiscale modeling with long-range electrostatic interactions in ionic solids, J. Mech. Phys. Solids **62**, 137 (2014).

[22] H. S. Park, M. Devel, and Z. Wang, A new multiscale formulation for the electromechanical behavior of nanomaterials, Comput. Methods Appl. Mech. Eng. **200**, 2447 (2011).

[23] W. Sun, S. B. Wang, J. Ng, L. Zhou, and C. T. Chan, Analytic derivation of electrostrictive tensors and their application to optical force density calculations, Phys. Rev. B **91**, 235439 (2015).

[24] S. Wang, J. Ng, M. Xiao, and C. T. Chan, Electromagnetic stress at the boundary: Photon pressure or tension?, Sci. Adv. **2**, e1501485 (2016).

[25] V. A. Markel, Numerical investigation of electrostatic force density in ionic crystals such as NaCl, Phys. Rev. B **107**, 104307 (2023).

[26] F. A. Reich, Coupling of continuum mechanics and electrodynamics: An investigation of electromagnetic force models by means of experiments and selected problems, Ph.D. thesis, Technische Universität Berlin, 2017.

[27] W. Rickert, An investigation of the electromagnetic coupling problem by means of a rational framework and selected experiments, Ph.D. thesis, Technische Universität Berlin, 2023.

[28] S. R. de Groot and L. G. Suttorp, *Foundations of Electrodynamics* (North-Holland Publishing Company, Amsterdam, 1972).

[29] A. C. Eringen and G. A. Maugin, *Electrodynamics of Continua I: Foundations and Solid Media* (Springer-Verlag, New York, 1990).

[30] C. Rinaldi and H. Brenner, Body versus surface forces in continuum mechanics: Is the Maxwell stress tensor a physically objective Cauchy stress?, Phys. Rev. E **65**, 036615 (2002).

[31] A. W. Behnke, T. J. Pollei, and K. J. Webb, Einstein–Laub and Lorentz optical force densities with a planar interface, Phys. Rev. A **108**, 033708 (2023).

[32] N. C. Admal and E. B. Tadmor, A unified interpretation of stress in molecular systems, J. Elast. **100**, 63 (2010).

[33] H. J. H. Clercx and G. Bossis, Electrostatic interactions in slabs of polarizable particles, J. Chem. Phys. **98**, 8284 (1993).

[34] N. Wang, S. Wang, Z.-Q. Zhang, and C. T. Chan, Closed-form expressions for effective constitutive parameters: Electrostrictive and magnetostrictive tensors for bianisotropic metamaterials and their use in optical force density calculations, Phys. Rev. B **98**, 045426 (2018).

[35] L. Cui, N. Wang, and J. Ng, Computation of internal optical forces using the Helmholtz tensor, Phys. Rev. A **104**, 013508 (2021).

[36] M. Mansuripur, A. R. Zakharian, and E. M. Wright, Electromagnetic-force distribution inside matter, Phys. Rev. A **88**, 023826 (2013).

[37] B. S. Park, H. S. Choi, J. O. Park, J. H. Wang, and I. H. Park, Equality of the Kelvin and Korteweg–Helmholtz force densities inside dielectric materials, IEEE Trans. Magn. **56**, 7515004 (2020).

[38] V. V. Datsyuk and O. R. Pavlyniuk, Maxwell stress on a small dielectric sphere in a dielectric, Phys. Rev. A **91**, 023826 (2015).

[39] J. R. Melcher and G. I. Taylor, Electrohydrodynamics: A review of the role of interfacial shear stresses, Annu. Rev. Fluid Mech. **1**, 111 (1969).

[40] D. A. Saville, Electrohydrodynamics: The Taylor–Melcher leaky dielectric model, Annu. Rev. Fluid Mech. **29**, 27 (1997).

[41] P. Penfield, Jr., and H. A. Haus, *Electrodynamics of Moving Media* (MIT Press, Cambridge, MA, 1967).

[42] A. Zangwill, *Modern Electrodynamics* (Cambridge University Press, Cambridge, 2013).

[43] R. N. C. Pfeifer, T. A. Nieminen, N. R. Heckenberg, and H. Rubinsztein-Dunlop, Colloquium: Momentum of an electromagnetic wave in dielectric media, Rev. Mod. Phys. **79**, 1197 (2007).

[44] J. D. Jackson, *Classical Electrodynamics*, 3rd ed. (Wiley, New York, 1999).

[45] S. M. Barnett and R. Loudon, On the electromagnetic force on a dielectric medium, J. Phys. B **39**, S671 (2006).

[46] B. Anghinoni, M. Partanen, and N. G. C. Astrath, The microscopic Ampère formulation for the electromagnetic force density in linear dielectrics, Eur. Phys. J. Plus **138**, 1034 (2023).

[47] J. A. Stratton, *Electromagnetic Theory* (McGraw-Hill, New York, 1941).

[48] H. A. Lorentz, *The Theory of Electrons and its Applications to the Phenomena of Light and Radiant Heat*, 2nd ed. (Dover Publications, New York, 1952), republication of the 2nd edition originally published by Teubner, Leipzig, 1916.

[49] S. P. Xiao and T. Belytschko, A bridging domain method for coupling continua with molecular dynamics, Comput. Methods Appl. Mech. Eng. **193**, 1645 (2004).

[50] R. E. Miller and E. B. Tadmor, A unified framework and performance benchmark of fourteen multiscale atomistic/continuum coupling methods, Model. Simul. Mater. Sci. Eng. **17**, 053001 (2009).

[51] N. Wang, S. Wang, and J. Ng, Electromagnetic stress tensor for an amorphous metamaterial medium, Phys. Rev. A **97**, 033839 (2018).

[52] M. Partanen, B. Anghinoni, N. G. C. Astrath, and J. Tulkki, Time-dependent theory of optical electro- and magnetostriction, Phys. Rev. A **107**, 023525 (2023).

[53] D. Katusele, C. Majidi, P. Sharma, and K. Dayal, Exploiting instabilities to enable large shape transformations in dielectric elastomers, Phys. Rev. Appl. **23**, 014007 (2025).

[54] S. Torza, R. G. Cox, and S. G. Mason, Electrohydrodynamic deformation and burst of liquid drops, Philos. Trans. R. Soc. A **269**, 295 (1971).

[55] B. Schulte Westhoff, Reproducibility code for electromagnetic local-load non-closure witnesses: common-grid correction, Zenodo (2026), version 0.2.0, 10.5281/zenodo.22903443